# Order–disorder phase boundary between ice VII and VIII obtained by first principles

Koichiro Umemoto [a,*], Renata M. Wentzcovitch [b], Stefano de Gironcoli [c], Stefano Baroni [c]

[a] Department of Geology and Geophysics, University of Minnesota, 421 Washington Ave., SE, Minneapolis, MN 55455, USA
[b] Minnesota Supercomputing Institute and Department of Chemical Engineering and Materials Science, University of Minnesota, 421 Washington Ave., SE, Minneapolis, MN 55455, USA
[c] Scuola Internazionale Superiore di Studi Avanzati (SISSA) and INFM DEMOCRITOS National Simulation Center, I-34014 Trieste, Italy

## ARTICLE INFO

## ABSTRACT

We report fundamental progress in the description of an archetypical hydrogen-bonded system: $H_2O$–ice. We calculated by first principles the ice VII–VIII phase boundary, an order–disorder phase boundary, by performing a complete sampling of configurations in a 16-molecule supercell. Vibrational effects are included within quasiharmonic theory. Several important features were successfully described: negative Clapeyron slope, isotope effect, and nearly-constant $T_c$ at low pressures. The equation of state was very well described below 40 GPa. Inclusion of tunneling effects and increase of supercell size should decrease the remaining discrepancies, i.e., the overestimation of volume above ∼40 GPa and the underestimation of $T_c$.

## 1. Introduction

Ice has a very rich phase diagram [1]. So far 16 crystalline phases have been identified experimentally. This richness originates in part in hydrogen order–disorder transitions such as Ih–XI [2], III–IX [3], VII–VIII [4], V–XIII, and XII–XIV [5], and VI–XV [6]. It is very difficult to determine experimentally such order–disorder phase boundaries at low pressures ($P$) and temperatures ($T$) since reorientation of water molecules in pure ice is severely suppressed (hysteresis). Hence, theoretical studies can be very helpful but they also have their intrinsic challenges. In particular, the phase boundary between ice VII (disordered) and VIII (ordered) is a good target for theoretical approaches for a couple of reasons: (i) they are typical forms of high density ice and density functional calculations are more successful in addressing these phases [7,8]; (ii) this phase boundary has been well constrained experimentally in a wide pressure range [9,10]. The main difficulty for theories is the calculation of the free energy and entropy in hydrogen-disordered ice VII. The most comprehensive study of the phase diagram of ice [11] was carried out quite successfully using empirical model potentials (TIP4P and SPC/E) using the ideal Pauling entropy [12] in fully hydrogen disordered phases, with a correction [13] for partially-disordered phases. The TIP4P model potential [14] was able to capture the main features of the experimental phase diagram of $H_2O$ at low pressures, but failed to reproduce the negative Clapeyron slope observed experimentally for ice VII–VIII transition. Other previous first-principles studies determined the transition temperature ($T_c$) at only one volume (at ∼2.4 GPa). Free energies were calculated by Metropolis Monte Carlo simulations with a

graph-invariant expansion [15,16] or by using a complete statistical sampling of possible molecular orientations [17,18] for various supercell sizes. However, these studies did not consider the vibrational contribution to the free energy, a necessary ingredient to compute finite-$T$ equations of states and phase boundaries. In this Letter, we present the first determination of an order–disorder phase boundary in $H_2O$ ice by first principles. The ice VII–VIII boundary is calculated over a wide pressure range (0–70 GPa) by performing a complete sampling of the ensemble of molecular configurations generated by a 16-molecule supercell. The partition function is then computed taking into account vibrational states. This approach successfully reproduces important observables: the room-$T$ equation of state of ice VII, the negative Clapeyron slope, and the isotope effect. It also offers an insight on the transition mechanism.

## 2. Methods

### 2.1. Statistical treatment

Ice VII and VIII consist of two interpenetrating hydrogen-bond networks, each one containing oxygens at the sites of a diamond lattice [4] (Figure 1a). Ice VII is hydrogen-disordered and paraelectric. Its oxygen sublattice is bcc with two molecules per cell. Ice VIII is hydrogen-ordered and antiferroelectric with dipole moments oriented in opposite directions in each of the networks. Its unit cell is body-centered tetragonal with four molecules. Hydrogen-disordered ice VII was modeled using a 16-molecule supercell ($2 \times 2 \times 2$ unit cells). This supercell consists of two interpenetrating ice Ic lattices (Figure 1a). The 8-molecule supercell of ice Ic has 90 possible hydrogen configurations compatible with the ice rules [12]. Among them, only 4 configurations are symmetrically distinct

* Corresponding author.
E-mail address: umemoto@cems.umn.edu (K. Umemoto).
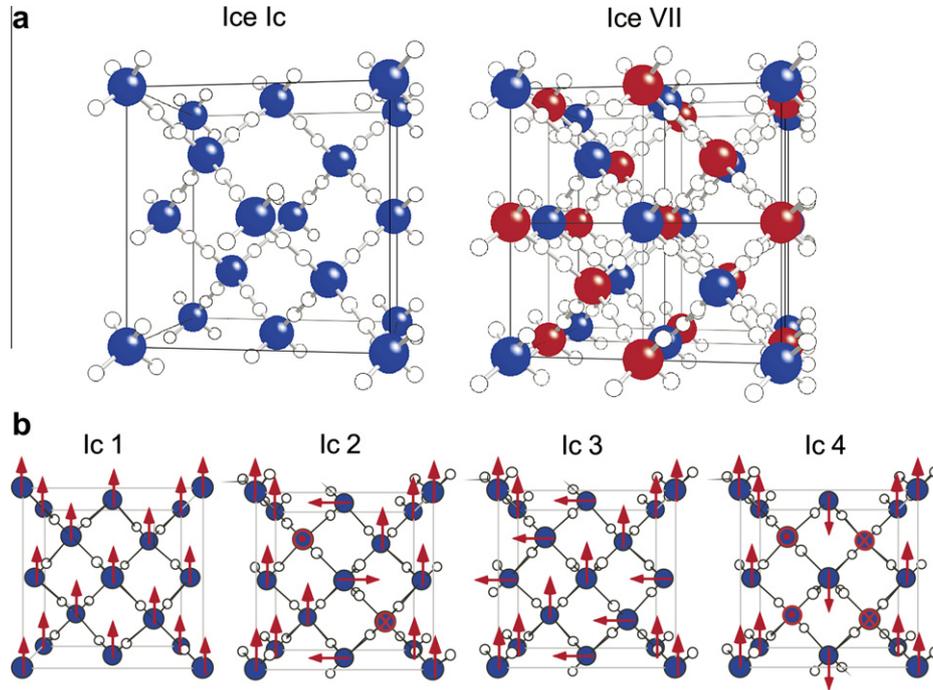
**Figure 1.** (a) The unit cell of ice Ic and the $2 \times 2 \times 2$ supercell of ice VII. Large blue and red spheres denote oxygen atoms. Small white spheres denote hydrogen atoms with the occupancy of 0.5. (b) Four distinct hydrogen configurations of ice Ic supercells containing 8 molecules. Red arrows denote dipole moments (**d**) on each molecule. Total dipole moments of these configurations are $(0,0,8)d, (0,0,4)d, (0,4,4)d$, and $(0,0,0)d$ (and their symmetrically-equivalent ones) respectively. (For interpretation of references to colors in this figure legend, the reader is referred to see the web version of this article.)

[19] (Ic 1–4 in Figure 1b). The 16-molecule ice VII supercell has 8100 (= 90 × 90) possible hydrogen configurations. Among them, only 52 configurations are symmetrically distinct. Antiferroelectric ice VIII (which will be referred to as Conf. 1) can be generated by interpenetrating two ice Ic 1s with dipole moments oriented in opposite directions. The static partition function then is:

$$Z_{\text{static}}(V,T) = \sum_{i=1}^{52} w_i \exp\left(-\frac{E_i(V)}{k_B T}\right), \tag{1}$$

where $E_i(V)$ and $w_i$ are the total energy and degeneracy of the $i$th symmetrically inequivalent configuration ($\sum_{i=1}^{52} w_i = 8100$), and $k_B$ is Boltzmann's constant. Within the quasi-harmonic approximation (QHA) [20], inclusion of non-interacting vibrational states changes the partition function to:

$$
\begin{aligned}
Z_{\text{QHA}}(V,T) &= \sum_{i=1}^{52} w_i \sum_{n_{s,i}=0}^{\infty} \exp\left\{ -\frac{1}{k_B T}\left( E_i(V) + \sum_{s=1}^{144} \frac{1}{2}\hbar\omega_{s,i}(V)\right)\right\} \\
&\quad \times \exp\left(-\frac{1}{k_B T}\sum_{s=1}^{144} n_{s,i}\hbar\omega_{s,i}\right) \\
&= \sum_{i=1}^{52} w_i \exp\left\{ -\frac{1}{k_B T}\left( E_i(V) + \sum_{s=1}^{144} \frac{1}{2}\hbar\omega_{s,i}(V)\right)\right\} \\
&\quad \times \prod_{s=4}^{144}\left\{ 1 - \exp\left(-\frac{\hbar\omega_{s,i}(V)}{k_B T}\right)\right\}^{-1}, \tag{2}
\end{aligned}
$$

where $\omega_{s,i}(V)$ and $n_{s,i}$ are the $s$th phonon frequency and the corresponding number of excited phonons for the $i$th configuration. The summation and the product over $s$ in Eq. (2) come from the zero-point motion (ZPM) and thermal excitation of phonon, respectively. From $Z(V,T)$, we can compute thermodynamical quantities: free energy $F(V,T) = -k_B T \ln Z$, entropy $S(V,T) = -(\partial F/\partial T)_V$, pressure $P(V,T) = -(\partial F/\partial V)_T$, Gibbs free energy $G(V,T) = F + PV$ (or

converted to $G(P(V,T),T)$), constant-pressure heat capacity $C_p(P,T) = -T(\frac{\partial^2 S}{\partial T^2})_P$, and so forth.

The temperature at the peak of the constant pressure heat capacity ($C_p$) should give the transition temperature ($T_c$) between ice VII and VIII. The pressure dependence of the temperature at the peak of $C_p$ gives the ice VII–VIII phase boundary. We investigated $C_p$ with and without vibrational contributions to $F$. The peak in $C_p$ originates in the static/configurational part of $F$. It is not very sharp for the relatively small number of configurations generated by the 16-molecule supercell, and the peak temperature strongly depends on the supercell size. Its full width at the half maximum (FWHM) is over 100 K at 10 GPa (Figure 2a). The FWHM decreases with increasing supercell size. Peak temperatures corresponding to 8- and 16-molecule supercells are 220 K and 193 K, respectively
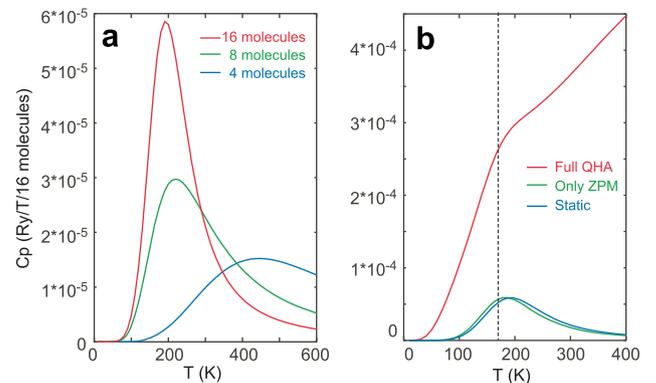


**Figure 2.** (a) Static heat capacity calculated at 10 GPa for 4, 8, and 16 molecule supercells. (b) Heat capacity calculated at 10 GPa: full $C_p$ including the vibrational contribution to the free energy, including ZPM contribution only and pure static calculations. The dashed vertical line denotes peak position with inclusion of ZPM energy only.

(Figure 2a). In the 16-molecule supercell, the peak is sharp enough to estimate $T_c$. The inclusion of vibrational effects turns the peak into a hump in the full heat capacity curve. The vibrational contribution to $C_p$ (within the QHA) increases rapidly around the peak temperature and the full heat capacity becomes inconspicuous (Figure 2b). This hump is caused by the phase transition but it is difficult to determine its precise position. An infinitely large supercell would produce a very sharp peak in $C_p$, which would not be affected by the background produced by the vibrational contribution to $C_p$. We therefore determined the peak in $C_p$ neglecting the thermally excitation of phonons (the product factor in Eq. (2)). We keep, however, the contribution from ZPM energy since its effect is noticeable (see Figure 2b). The positions of the hump and the peak of two $C_p$ with and without the thermally excitation of phonons are almost identical to each other.

## 2.2. Computational details

We calculated by first principles the total energies $E_i(V)$ and phonon frequencies $\omega_{s,i}(V)$ of all 52 configurations. We used norm-conserving pseudopotentials [21] and the Perdew–Burke–Ernzerhof (PBE) functional [22] for the exchange–correlation (XC). A plane-wave basis set with a cutoff energy of 100 Ry and a $2 \times 2 \times 2$ **k**-point mesh were adopted for all supercells. Lattice constants and atomic positions were fully optimized by using a damped form of variable-cell-shape dynamics [23,24] at static pressures of −1, 0, 10, 30, 50, 70 GPa. Phonon frequencies were computed using density-functional perturbation theory [25,26]. In Eq. (2), we sampled zone-center phonon modes ($\Gamma$-point). Because of the zone folding, zone-center phonon modes in the present 16-molecule supercell comprise zone-center and zone-edge modes in the 2-molecule unit cell. We calculated $C_p$s at several pressures for ice VIII in the 16-molecule supercell by Eq. (2) with $w_i = \delta_{i,1}$ (i.e., 1 for ice VIII and 0 for other configurations) and zone-center phonon sampling. They agreed well with $C_p$s calculated for ice VIII in the 4-molecule body-centered-tetragonal unit cell with a well-converged phonon sampling on $8 \times 8 \times 8$ **q** mesh; differences in $C_p$ between two cells were found to be less than 5%. This result supports the validity of the zone-center phonon sampling in the 16-molecule supercell.
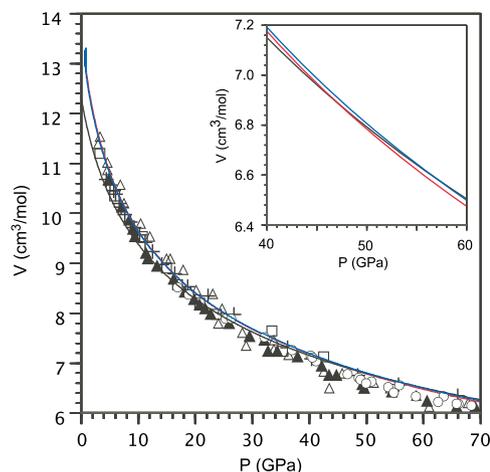
## 3. Results and discussion

### 3.1. Phase boundary

Calculated parameters of a third-order Birch–Murnaghan equation of state (EOS) for ice VII at 300 K are shown in Table 1. Figure 3 shows the calculated EOS reproduces well experimental raw data points below ∼40 GPa, supporting the validity of our computational method again. Vibrational effects are quite important and increase the equilibrium volume at 0 GPa by more than 10% at 300 K. ZPM is responsible for most of this change. This is the standard type of ZPM effect. In normal stable solids, phonon frequencies tend to increase in average with decreasing $V(P)$ ($\frac{\partial \omega_i}{\partial V} < 0$). Therefore, ZPM correction on the static $P$, $\Delta P_{ZPM}$, is positive ($\Delta P_{ZPM} = -\sum_i \frac{1}{2}\hbar \frac{\partial \omega_i}{\partial V}$) and $V(P)$ increases. This is observed in ice VII and VIII at lower pressures but changes at higher pressures



**Figure 3.** Static compression curve (black line) and 300 K analogs of $H_2O$ (red line) and $D_2O$ (blue line). Crosses, filled triangles, open triangles, squares, and circles denote experimental data for $H_2O$ by Hemley et al. [27], Wolanin et al. [28], Loubeyre et al. [29], Somayazulu et al. [30], and Sugimura et al. [31], respetively. (For interpretation of references to colors in this figure legend, the reader is referred to see the web version of this article.)

($P \gtrsim 50$ GPa). Vibrational effects *decrease* V because at high pressures stretching mode frequencies decrease very rapidly [9,32,10] with decreasing volume (see Figure 3 inset). This well-known effect is associated with the strengthening of hydrogen bonds (O···H) and weakening of the covalent (intramolecular) bonds (O–H). The positive $\frac{\partial \omega_i}{\partial V}$ of the stretching modes predominate over those of other modes, $\Delta P_{ZPM}$ becomes negative, and $V(P)$ decreases. This effect is stronger in $H_2O$ than in $D_2O$ (see Figure 3 inset).

As shown in Figure 3, calculated $V(P)$ is larger than experimental $V(P)$ above ∼40 GPa. This overestimation may be caused primarily by the neglect of proton tunneling between double potential wells. Experimentally an anomalous volume shrinkage was observed between ∼40 and ∼70 GPa [27,29,31,33,34], corresponding to the transition between ice VII/VIII to VII′ and then ice X; ice VII′ is the dynamically-disordered form of ice VII/VIII. Theoretically tunneling was shown to be crucial for describing this transition [35]. Therefore, inclusion of tunneling should further decrease $V(P)$ and improve agreement with experimental values.
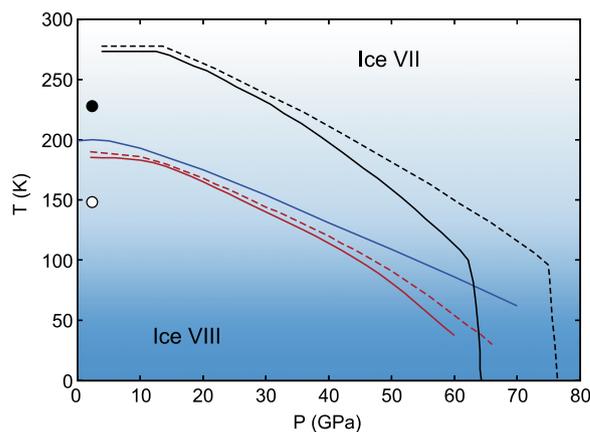


**Figure 4.** Calculated ice VII–VIII phase boundaries (blue line: static, red lines: QHA results). Black solid and dashed lines are experimental phase boundaries for $H_2O$ and $D_2O$ by Song et al. [10]; their nearly vertical parts are phase boundaries between ice VIII and VII′. Black and white dots are $T_c$ calculated using the BLYP-type XC functional by Refs. [15,16] and [17,18], respectively. (For interpretation of references to colors in this figure legend, the reader is referred to see the web version of this article.)

**Table 1**
Calculated equation of state (Birch–Murnaghan) parameters of ice VII at 300 K.

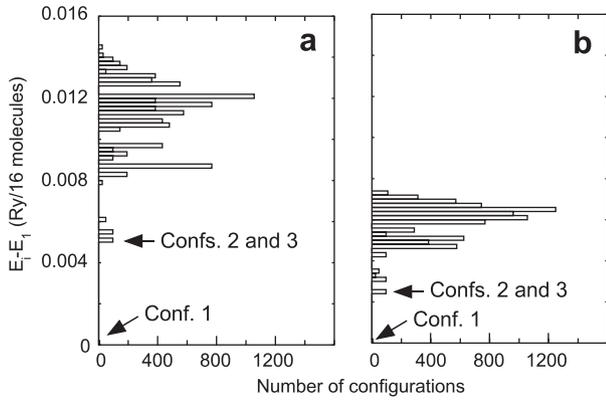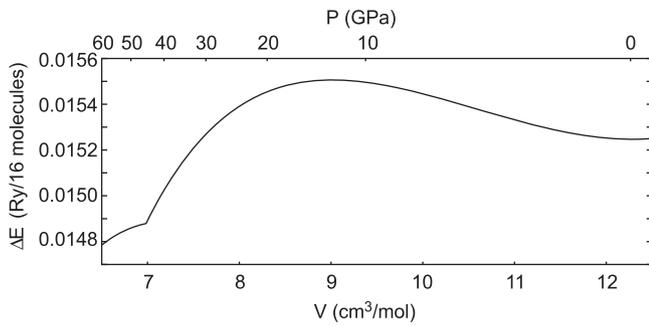|  | $V_0$ (cm³/mol) | $B_0$ (GPa) | $B_0'$ |
|---|---|---|---|
| Static | 12.28 | 18.68 | 5.02 |
| QHA, $H_2O$ | 13.53 | 12.68 | 4.96 |
| QHA, $D_2O$ | 13.52 | 12.51 | 5.06 |

**Figure 5.** Histograms of the total energy $E_i(V)$ at several volumes at (a) 10.32 cm$^3$/mol ($\sim$5 GPa) and (b) 6.79 cm$^3$/mol ($\sim$50 GPa).



**Figure 6.** Energy distribution: $\Delta E(V) = \max_{1 \leqslant i \leqslant 52}(E_i) - \min_{1 \leqslant i \leqslant 52}(E_i)$.

Figure 4 shows the ice VII–VIII phase boundary for H$_2$O and D$_2$O determined from the peak position in $T$ of $C_p(P,T)$. These phase boundaries reproduce two experimentally observed properties: the negative Clapeyron slope at medium and high $P$s ($\gtrsim$ 10 GPa) and the nearly constant $T_c$ at low $P$. These results are related to the distribution of $E_i(V)$ of the 52 configurations (Figures 5 and 6). When the width of the $E_i(V)$ distribution is large, i.e., $\Delta E = \max_{1 \leqslant i \leqslant 52}(E_i) - \min_{1 \leqslant i \leqslant 52}(E_i)$ is large, the configuration entropy of ice VII is relatively small and $T_c$ is high. Similarly, when $\Delta E$ is small, $T_c$ is low. With decreasing volume ($\lesssim$ 9 cm$^3$/mol) (or

increasing $P$) all atomic configurations converge to a single one, that of ice X, and $\Delta E$ decreases (Figure 6). This leads to a negative Clapeyron slope at high $P$s. In contrast, at large volumes ($\gtrsim$ 9 cm$^3$/mol), $\Delta E$ is weakly dependent of volume, producing nearly constant $T_c$ at low $P$s. As expected, vibrational effects on $T_c$ and on $V$ are larger in H$_2$O than in D$_2$O. Consequently, the isotope effect on $T_c$ is well reproduced; D$_2$O has higher $T_c$ than H$_2$O (Figure 4).

### 3.2. Transition mechanism

The probability of occurrence of the $i$th configuration is given by

$$p_i(V,T) = \frac{w_i \exp\left(-\frac{E_i(V)}{k_B T}\right)}{Z(V,T)}, \qquad (3)$$

or $p_i(P,T)$ after $V \to P(V,T)$ conversion. Figure 7a shows $p_i(P,T)$ for the 52 configurations at 10 GPa. At very low $T$ the probability of ice VIII, $p_1$, is nearly 1 since Conf. 1 has the lowest energy among all configurations (Figure 5). As $T$ increases, $p_1$ decreases while $p_2$ and $p_3$ increase. Conf. 2(3) consists of two interpenetrating lattices, Ic 1 and Ic 2(3) (see Figure 1b). Confs. 2 and 3 have the second and third lowest energy in static calculations. This means that with increasing $T$ molecular reorientation starts in a single sub-lattice of ice VIII, leaving the other sub-lattice unchanged. With increasing $T$ molecular reorientation spreads over both sub-lattices until the transition to ice VII is completed. Conversely, ice VII transforms into ice VIII through Confs. 2 and 3, i.e., hydrogen ordering develops in one of the sub-lattices first. At constant $T$, the probability of each configuration also varies with $P$. Figure 7b shows $p_i(P,T)$ of the 52 configurations at 300 K. With decreasing $P$, $p_1, p_2$, and $p_3$ increase considerably with respect to the probabilities of other configurations. The increase of $p_1$ at low $P$ suggests partial ordering of ice VII into VIII which may correspond to the $\sim \frac{1}{2}\frac{1}{2}\frac{1}{2}$ super-lattice reflection observed at 300 K below $\sim$25 GPa by X-ray diffraction experiments on ice VII [29]. The $\frac{1}{2}\frac{1}{2}\frac{1}{2}$ peak is forbidden in ice VII but corresponds to the 101 peak of ice VIII. The precise lowest energy configurations might differ from the configurations found here since the adopted supercell contains only 16 molecules. However, the present findings naturally suggest an interpretation for this experimental observation.
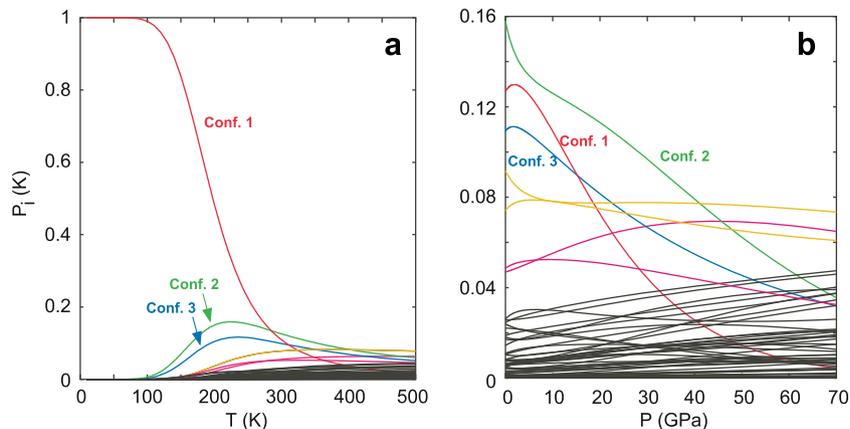


**Figure 7.** Probabilities of the 52 symmetrically inequivalent configurations generated by the 16-molecule supercell at: (a) 10 GPa and (b) 300 K. The most likely configurations are represented by color lines. Conf. 1 is ice VIII and consists of ice Ic 1 with the dipole moment $\mathbf{d} = (0,0,8)$ and Ic 1 with $\mathbf{d} = (0,0,-8)$. Conf. 2(3) consists of Ice Ic 1 with $\mathbf{d} = (0,0,8)$ in one sub-lattice of ice VII, and Ic 3 (Ic 2) with $\mathbf{d} = (0,4,-4)(\mathbf{d} = (0,0,-4))$ in the second sub-lattice (see Figure 1 for the definition of ice Ic configurations).

### 3.3. Potential improvements

Several aspects of this calculation could still be improved: inclusion of proton tunneling and anharmonic effects, increase of supercell size, and better treatment of XC functional. The abrupt drop of $T_c$ observed experimentally between ice VII/VIII and VII′ [9,32,10] is not reproduced here mainly because tunneling was neglected. Phonon frequencies were calculated in the harmonic approximation. However, anharmonicity increases with $P$ for oscillation in double-well potentials [36]. Also, $T_c$s obtained here are lower than the experimental values. Larger supercells could improve $T_c$. They can accommodate defective ice VIII structures which can contribute to increase its entropy and stability field. Previous calculations with the same XC functional (BLYP [37]) and density corresponding to ∼2.4 GPa showed that by increasing the supercell size from 16 [17,18] to 1024 molecules [15,16] $T_c$ increased by ∼80 K. Such difference would bring our results very close to the experimental phase boundary at low $P$ (Figure 4). However, the cell sizes in our calculation are too small for a reliable finite-size scaling analysis [38] of the results. In the present study we used the PBE-type XC functional which overestimates and underestimates O–H and O⋯H bondlengths respectively [7,8]. According to an extensive study of XC functionals [39], PBE1W, a GGA functional with one parameter of PBE tuned to reproduce the energetics of water clusters, and some meta-GGA and hybrid-GGA functionals can describe better than PBE O–H and O⋯H bonds. Therefore these functionals could improve the distribution of configurational energies (Figures 5 and 6) and consequently $T_c$. Despite all the possible improvements to our calculation, our results reproduce several features of an order–disorder phase boundary in ice, i.e., the negative Clapeyron slope, nearly flat $T_c$ at low $P$, and the isotope effect.

### Acknowledgments

### References

[1] V.F. Petrenko, R.W. Whitworth, Physics of Ice, Oxford University Press, Oxford, 1999.
[2] Y. Tajima, T. Matsuo, H. Suga, Nature 299 (1982) 810.
[3] J.D. Londono, W.F. Kuhs, J.L. Finney, J. Chem. Phys. 98 (1993) 4878.
[4] W.F. Kuhs, J.L. Finney, C. Vettier, D.V. Bliss, J. Chem. Phys. 81 (1984) 3612.
[5] C.G. Salzmann et al., Science 311 (2006) 1758.
[6] C.G. Salzmann, P.G. Radaelli, E. Mayer, J.L. Finney, Phys. Rev. Lett. 103 (2009) 105701.
[7] K. Umemoto, R.M. Wentzcovitch, Phys. Rev. B 69 (2004) 180103.
[8] K. Umemoto, R.M. Wentzcovitch, Phys. Rev. B 71 (2005) 012102.
[9] Ph. Pruzan, J. Mol. Struct. 322 (1994) 279;
     Ph. Pruzan et al., J. Phys. Chem. B 101 (1997) 6230.
[10] M. Song, H. Yamawaki, H. Fujihisa, M. Sakashita, K. Aoki, Phys. Rev. B 68 (2003) 014106.
[11] E. Sanz, C. Vega, J.L.F. Abascal, L.G. MacDowell, Phys. Rev. Lett. 92 (2004) 255701.
[12] L. Pauling, J. Am. Chem. Soc. 57 (1935) 2680.
[13] R. Howe, R.W. Whitworth, J. Chem. Phys 86 (1987) 6443.
[14] W.L. Jorgensen et al., J. Chem. Phys. 79 (1983) 926.
[15] S.J. Singer et al., Phys. Rev. Lett. 94 (2005) 135701.
[16] C. Knight et al., Phys. Rev. E 73 (2006) 056113.
[17] J.L. Kuo, M.L. Klein, J. Phys. Chem. B 108 (2004) 19634.
[18] J.L. Kuo, Phys. Chem. Chem. Phys. 7 (2005) 3733.
[19] J. Lekner, Physica B 240 (1997) 263.
[20] D. Wallace, Thermodynamics of Crystals, Wiley, New York, 1972.
[21] N. Troullier, J.L. Martins, Phys. Rev. B 43 (1991) 1993.
[22] J.P. Perdew, K. Burke, M. Ernzerhof, Phys. Rev. Lett. 77 (1996) 3865; Erratum. Phys. Rev. Lett. 78 (1996) 1396.
[23] R.M. Wentzcovitch, Phys. Rev. B 44 (1991) 2358.
[24] R.M. Wentzcovitch, J.L. Martins, G.D. Price, Phys. Rev. Lett. 70 (1993) 3947.
[25] P. Giannozzi, S. de Gironcoli, P. Pavone, S. Baroni, Phys. Rev. B 43 (1991) 7231.
[26] S. Baroni, S. de Gironcoli, A. Dal Corso, P. Giannozzi, Rev. Mod. Phys. 73 (2001) 515.
[27] R.J. Hemley et al., Nature 330 (1987) 737.
[28] E. Wolanin et al., Phys. Rev. B 56 (1997) 5781.
[29] P. Loubeyre et al., Nature 397 (1999) 503.
[30] M. Somayazulu et al., J. Chem. Phys. 128 (2008) 064150.
[31] E. Sugimura et al., Phys. Rev. B 77 (2008) 214103.
[32] A.F. Goncharov, V.V. Struzhkin, H.K. Mao, R.J. Hemley, Phys. Rev. Lett. 83 (1999) 1998.
[33] J. Hama, K. Suito, Phys. Lett. A 187 (1994) 346.
[34] C.S. Zha et al., J. Chem. Phys. 126 (2007) 074506.
[35] M. Benoit, D. Marx, M. Parrinello, Nature 392 (1998) 258.
[36] M. Bernasconi, P.L. Silvestrelli, M. Parrinello, Phys. Rev. Lett. 81 (1998) 1235.
[37] A.D. Becke, Phys. Rev. A 38 (1988) 3098;
     C. Lee, W. Yang, R.G. Parr, Phys. Rev. B 37 (1988) 785.
[38] M.E. Fisher, M.N. Barber, Phys. Rev. Lett. 28 (1972) 1516.
[39] E.E. Dahlke, D.G. Truhlar, J. Phys. Chem. B 109 (2005) 15677.
[40] P. Giannozzi et al., J. Phys.: Condens. Matter 21 (2009) 395502. http://www.quantum-espresso.org.